Amplification of Single Molecule Translocation Signal Using β-Strand Peptide Functionalized Nanopores

Yael Liebes-Peer,[†,‡,§,⊥] Hanna Rapaport,[†,§] and Nurit Ashkenasy[‡,§,*]

[†]Department of Biotechnology Engineering, [‡]Department of Materials Engineering, and [§]The Ilze Katz Institute for Nanoscale Technology, Ben-Gurion University of the Negev, P.O. Box 653, Beer-Sheva 84105, Israel. [⊥]Present address for Y.L.-P.: School of Chemistry, Tel Aviv University, P.O. Box 39040, 6997801, Israel.

ABSTRACT Changes in ionic current flowing through nanopores due to binding or translocation of single biopolymer molecules enable their detection and characterization. It is, however, much more challenging to detect small molecules due to their rapid and small signal signature. Here we demonstrate the use of *de novo* designed peptides for functionalization of nanopores that enable the detection of a small analytes at the single molecule level. The detection relies on cooperative peptide conformational change that is induced by the binding of the small molecule to a receptor domain on the peptide. This change results in alteration of the nanopore effective diameter and hence induces current perturbation signal. On the basis of this approach, we demonstrate here the detection of diethyl 4-nitrophenyl phosphate (paraoxon), a poisonous organophosphate molecule. Paraoxon binding is induced by the incorporation of the catalytic triad of acetylcholine esterase in the hydrophilic domain of a short amphiphilic peptide and promotes β-sheet assembly of the peptide both in solution and for peptide molecules immobilized on solid surfaces. Nanopores coated with this peptide allowed the detection of paraoxon at the single molecule level revealing two binding arrangements. This unique approach, hence, provides the ability to study interactions of small molecules with the corresponding engineered receptors at the single molecule level. Furthermore, the suggested versatile platform may be used for the development of highly sensitive small analytes sensors.

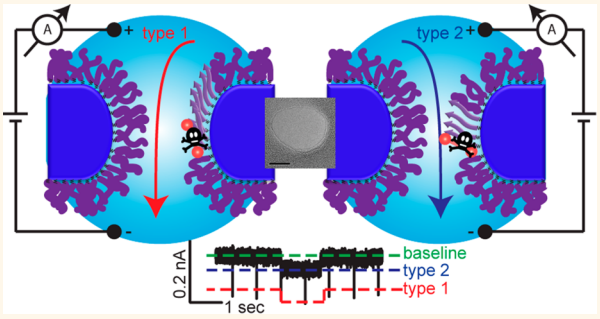

KEYWORDS: solid state nanopore · β-sheet · peptides · single molecule detection · paraoxon · biosensor · *de novo* designed peptide

Nanopores have gained a lot of interest in recent years due to the ability to use them for the detection of biomolecules at the single molecule level, obtained by monitoring changes in ionic current flowing through the nanopore, which are induced by the molecule's translocation through the nanopore or binding to the nanopore rims.[1−3] Analysis of the magnitude and duration of the current perturbation event and the frequency of events provides both quantitative and qualitative analytical information.[4,5] While early studies utilized biological nanopores,[4,6,7] to overcome robustness and size limitations, methodologies to prepare single nanopores in solid state membranes have been developed. Additional advantages of these artificial nanopores include the ability to control their shape and prospective integration into lab-on-a-chip devices.[7−9] Such solid state nanopores have proven to be useful for the detection of DNA[10,11] and proteins.[12−15] In particular, large efforts have been devoted to the development of a DNA sequencing machine based on such chips.[11,16] However, the detection of small molecules, which is possible when using biological nanopores,[17−21] is hampered in solid state nanopores due to incompatibility of the nanopore size and the temporal resolution of the measurement with the molecule size and its translocation duration, respectively. This limits the use of such nanopores for the detection of, *e.g.*, hormones, peptides and small poisonous molecules, such as organophosphates.[4,7] Recent studies have demonstrated that the presence of small molecules in solid state nanopores can be sensed if these induce significant changes to organic layer sensitizing the nanopore. For example, disintegration of a complex DNA supersandwich structure

* Address correspondence to nurita@bgu.ac.il.

Received for review March 7, 2014 and accepted June 20, 2014.

Published online June 20, 2014
10.1021/nn501331u

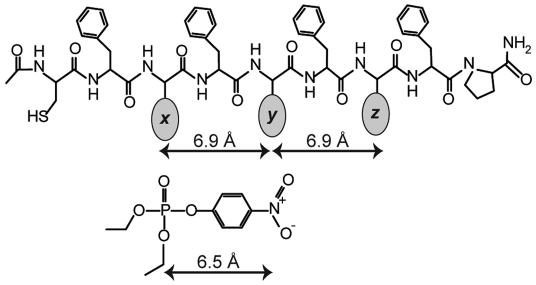

β-ESH: Ac-Cys-Phe-Glu-Phe-Ser-Phe-His-Phe-Pro-NH_2
β-HES: Ac-Cys-Phe-His-Phe-Glu-Phe-Ser-Phe-Pro-NH_2
β-EHS: Ac-Cys-Phe-Glu-Phe-His-Phe-Ser-Phe-Pro-NH_2
R-PEP: Ac-Cys-Ser-Pro--Phe-Phe-Glu-His-Phe-Phe-NH_2

Scheme 1. Structure of the β-sheet forming peptides and paraoxon.

tethered to a nanopore in the presence of adenosine triphosphate (ATP) was shown to result in pronounced increase in the conductance of the nanopore.[22] A similar effect was achieved by a substantial conformational effect induced to a Zinc finger peptide monolayer in the presence of Zinc.[23] However, these processes do not provide single molecule sensitivity, which is presented in biological nanopores utilizing host guest interactions.[24−26]

We have postulated that the detection of binding of small molecules at the single molecule level can be achieved if the binding of the molecule would induce pronounced and long-range conformational change of a receptor layer functionalizing the nanopore, a process that would invoke a detectable change in the current. As an analyte to test this hypothesis we have chosen to work with organophosphate molecules. This is since organophosphates, which are routinely used as pesticides, are known to be extremely toxic to humans and the ecosystem in general due to their ability to bind irreversibly to the active site of acetylcholinesterase (AChE, acetylcholine hydrolase, EC 3.1.1.7).[27,28] The toxicity of organophosphates molecules makes them also dangerous nerve gases in biochemical warfare. Hence, an ongoing pursuit for improved, rapid, selective and sensitive detection techniques of organophosphates is being conducted.[29−31] Routine detection techniques are based on conventional mass spectroscopy and gas or liquid chromatography methods.[32,33] However, these methods suffer from several disadvantages, including low detection limit, prolonged assay time, expensive equipment, and the requirement for highly trained personnel.[34] Enzyme-based biosensors are becoming highly attractive;[35−38] however, these present several limitations such as need to purify a whole enzyme, loss of activity during immobilization and long distance between the active site and the transducer site (due to the dimensions of the enzyme) that may reduce assay sensitivity.

We show here *de novo* designed peptides that allow the detection of diethyl 4-nitrophenyl phosphate (paraoxon), a model organophosphate molecule, at the single molecule level. The peptide design is based on the incorporation of the catalytic amino acids triad, His, Glu and Ser, from the active site of AChE into a β-sheet forming sequence.[39] Characterizations of paraoxon binding to the peptide and the induced assembly of the peptides to β-sheets in solution and as monolayers on gold and silicon nitride surfaces were used to screen for the optimal peptide receptor sequence. Monitoring the ionic current passing through peptide functionalized nanopores allowed detection of single paraoxon molecule binding and revealed two current event signatures, indicating two different binding arrangements. These results demonstrate the feasibility of using nanopore functionalized with specifically designed peptide receptors for the detection of small molecules at the single molecule level.

RESULTS AND DISCUSSION

Paraoxon Receptor Design. We have postulated that both signal and temporal sensitivity limitations for the detection of small molecules by solid state nanopores can be overcome by designing a specific receptor layer that undergoes long-range cooperative change due to molecule binding. The ongoing need to develop sensors for organophosphates made us choose them as the analyte molecules. AChE active site, to which organophosphates bind, consists of a catalytic amino acids triad, His, Glu and Ser, which are in close proximity and planar arrangement.[27,28] In a recent work these three amino acids were embedded in an amphiphilic β-strand peptide motif, and it was demonstrated that the peptides have higher tendency to form β-sheets at the air water interface in the presence of a model (less toxic) organophosphate, paraoxon.[39] We have, therefore, hypothesized that paraoxon binding may induce long-range folding that may be detected by changes in the ionic current flowing through nanopores functionalized with a monolayer of such peptides. The peptides consisted of an alternating sequence of hydrophobic and hydrophilic amino acids that can assemble into β-sheet (Scheme 1),[40,41] where the hydrophilic domain (X, Y and Z positions) included three combinations of the AChE catalytic triad, His, Glu and Ser,[39] in order to select the optimal paraoxon receptor peptide. We note that the 6.9 Å distances of X−Y or Y−Z amino acids in the sequence is similar to the 6.5 Å distance between N and P atoms in paraoxon (Scheme 1), probably giving rise to the observed

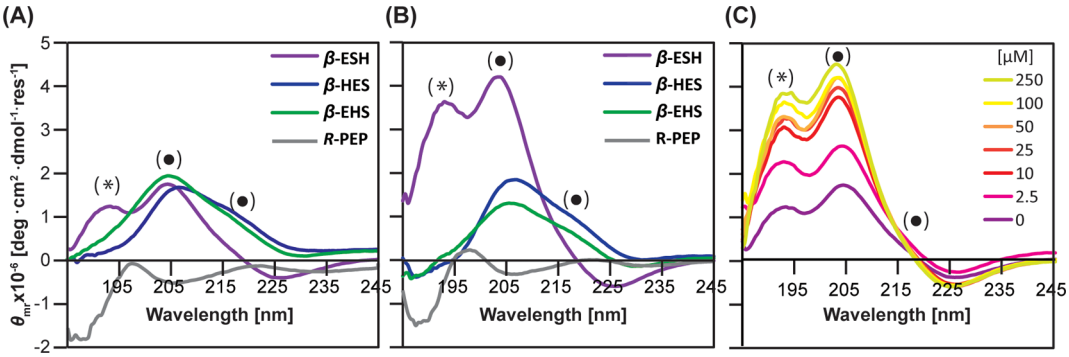

Figure 1. CD spectra of peptides with and without paraoxon. (A) CD spectra of 100 μM peptides *β*-ESH, *β*-HES, *β*-EHS and R-PEP without paraoxon. (B) CD spectra of each of the peptides (100 μM) in the presence of 100 μM paraoxon. (C) Elipticity of *β*-ESH with increasing paraoxon concentration. Spectra were recorded in 1:1 triple deionized water:acetonitrile solution. β-sheet peak at ~193 nm is marked by (*), and the L-Phe ring peak at 204 nm and knee at 217 nm are marked by (●).

interactions.[39] In order to afford the use of these sequences to functionalize nanopores, cysteine was added at the N-terminus of the peptide to provide a free thiol group, which can be used to bind the peptide to the surface (Scheme 1). The peptides were acetylated and amidated at the N- and C-termini, respectively, in order to prevent electrostatic interactions between peptide molecules. An additional peptide, **R-PEP**, with the same amino acids but in a scrambled sequence, which is thus not expected to bind paraoxon, nor adopt the β-sheet structure upon assembly, was used as a control.

Peptide—Paraoxon Interactions in Solution. The ability of the four designed peptides to react with paraoxon molecule in solution was studied using circular dichroism (CD). The spectra of ***β*-EHS** and ***β*-HES** (Figure 1A) exhibited a broad positive peak at 204 nm and a shoulder at 217 nm, attributed to aromatic stacking of Phe residues in solutions.[42−44] The appearance of an additional peak at 193 nm for ***β*-ESH** indicates significant folding of this peptide into β-sheets (Figure 1A). This is supported by the reduction of the peak at 217 nm due to a convoluted contribution of a negative valley at 215 nm, typical to β-sheet CD spectra. **R-PEP** showed a different and much weaker spectrum compared to the three other peptides, with a shallow minimum at 205 nm indicative of random coil conformation, as expected.

The introduction of 100 μM paraoxon to the peptides solution affected mostly the ellipticity of ***β*-ESH**, showing enhanced absorption of the peaks at 193 and 204 nm (Figure 1B). This enhancement in the ellipticity was found to depend on the concentration of paraoxon (Figure 1C). These results indicate that paraoxon binds effectively to ***β*-ESH**, by this promoting the assembly of the peptide into β-sheets. This is further confirmed by the appearance of an isosbetic point at 213 nm, which manifests a direct transformation between two different peptide conformations. The three other peptides (***β*-HES**, ***β*-EHS** and **R-PEP**) exhibited much smaller changes in the spectra in the presence of paraoxon for the entire concentration range (Figures 1B and S1, Supporting Information). These results are in general agreement with the results observed for the uncapped peptides.[39] Hence, while paraoxon binding cannot be ruled out, for these three peptides minor conformational changes are induced in solution. This difference in the behavior can be associated with an intrinsic propensity of ***β*-ESH** to form pleated β-strands that is indicated in the CD of the neat peptides solutions. Binding of paraoxon to a peptide molecule within a β-sheet domain, apparently promotes further assembly of additional peptide molecules into the β-sheet. For peptide monolayers attached to a nanopore, this correlative effect results in a pronounced ionic current change, as will be shown below.

Paraoxon Binding to Peptide Monolayers. Peptide immobilization on silicon nitride surfaces was achieved by silanization of the surfaces with (3-aminopropyl-)triethoxysilane (APTES) to which the peptide was attached through *N*-γ-maleimidobutyryl-oxysulfosuccinimide ester (sulfo-GMBS) linker (Figure 2A, left side and Scheme S1, Supporting Information). First indications for interactions of paraoxon with peptides immobilized on silicon nitride surfaces were obtained by ellipsometry (Figure 2A). A thickness of 0.8 $\pm$ 0.2 nm and 1.0 $\pm$ 0.4 nm was found for APTES and sulfo-GMBS monolayers, respectively, in agreement with the estimated theoretical monolayer thicknesses. An increase of 3.0 $\pm$ 0.9 nm in the thickness of the organic layer was found after immobilization of ***β*-ESH** and ***β*-HES.** This indicates the formation of a dense peptide monolayer with an extended structure (theoretical length calculated to be 3.1 nm for fully extended β-strand[40]) at a vertical angle with respect to the surface. Immobilization of ***β*-EHS** resulted in slightly thinner add-layer, with thicknesses of about 2.6 $\pm$ 1.4 nm. A much thinner layer of about 1.5 $\pm$ 0.5 nm was formed for **R-PEP**. We attribute the formation of a thinner layer to lower coverage of the corresponding peptide. Contact angle measurements further confirmed peptide immobilization (Figure S2, Supporting Information).[45]

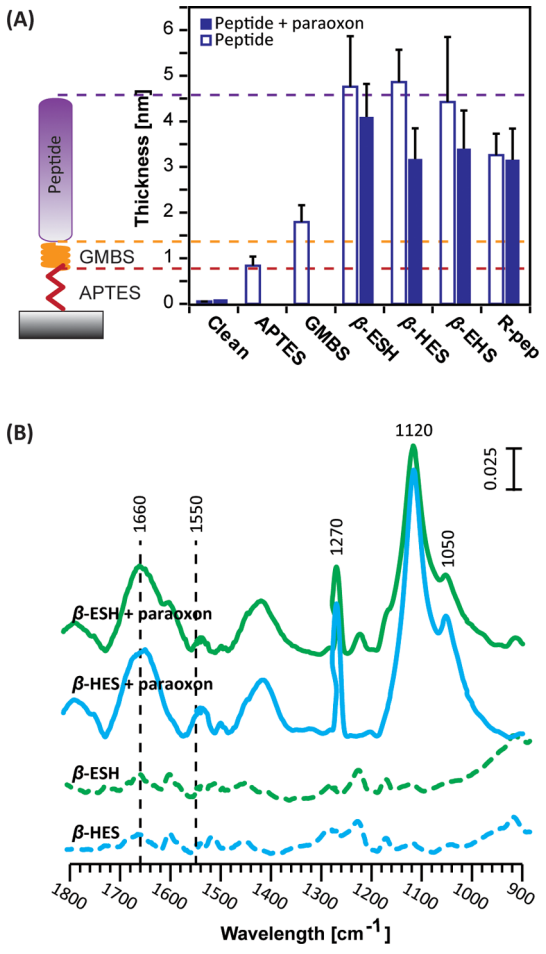

Figure 2. Structural characterizations of peptide monolayers assembled on silicon nitride and gold surfaces. (A) Monolayers' thickness, obtained by ellipsometry for peptide monolayers before and after exposure to paraoxon. Scheme of peptide arrangement on silicon nitride surface is provided to the left of the image. Dashed red, yellow and purple lines indicate theoretically estimated thickness values for APTES, sulfo-GMBS and peptide monolayers, respectively (theoretical length of the peptides was calculated assuming extended β-strand by 6.9 Å $\times$ number of amino acids $\times$ 0.5[40]). (B) Polarization modulation infrared reflection adsorption spectroscopy (PM-IRRAS) spectra of *β*-ESH and *β*-HES peptide monolayers on gold surfaces before and after paraoxon binding (spectra are shifted from each other for clarity). Bare gold background was subtracted from the spectra.

The thickness of the layers slightly decreased upon immersing the β-strand peptide modified surfaces in paraoxon solution (Figure 2A), indicating interactions between paraoxon molecules and the functionalized surfaces. The reduction in the thickness for monolayers with extended peptide conformations implies that the tilt angle of the peptides with respect to the surface increases due to paraoxon binding. In contrary, exposing surfaces modified with **R-PEP** to paraoxon solution did not result in a change in the thickness of the monolayer, suggesting insignificant binding of paraoxon to **R-PEP**. This experiment, however, confirms that the integrity of the organic layer is retained upon exposure to paraoxon; hence, the reduction in the thickness for the former peptides cannot be attributed to deterioration of the layer.

Further information on paraoxon binding was provided by X-ray photoelectron (XPS) measurements. For these measurements, peptides were immobilized on gold surfaces directly through the thiol side chain of the Cys residue. Binding was confirmed by ellipsometry and contact angle measurements, which indicated similar trends to these observed on silicon nitride surfaces (Figure S3, Supporting Information). The XPS measurements indicated carbon/nitrogen atomic ratio values that correspond to the peptides' chemical formula for all peptides (Table S1, Supporting Information). Paraoxon binding resulted in the appearance of a small phosphorus binding energy peak (P_{2p}, 138 eV). Rough estimation of the ratio between paraoxon and peptide molecules was obtained by the atomic ratio between sulfur and phosphorus, confirming significant binding of paraoxon to these monolayers (Table S1, Supporting Information). Only traces of paraoxon were detected for ***β*-EHS** and **R-PEP** monolayers, indicating less specific interactions of paraoxon with these peptide monolayers.

The evolution of the secondary structure of the peptides on the surface due to interactions with paraoxon was monitored using polarization modulation infrared reflectance absorption spectroscopy (PM-IRRAS). Very small signals were observed for the peptide monolayers before interactions with paraoxon molecules (Figure 2B and S4, Supporting Information), indicating that the monolayers are randomly orientated on the surface. Remarkable changes were observed in the spectra of ***β*-ESH** and ***β*-HES** monolayers after paraoxon binding (Figure 2B). Peaks attributed to the organophosphate group ν(P═O), C—O—P(═O) transitions at 1270 cm^{-1} and 1050 cm^{-1}, respectively, as well as a shoulder at 1025 cm^{-1} attributed to the ν(P—O—Et) transition, appeared in the spectra.[46] A strong peak at 1120 cm^{-1}, corresponding probably to both the phosphate group[46] and the benzyl ring of paraoxon, and peaks corresponding to its nitro group at 1410 cm^{-1} (ν-C—N) and 1614 cm^{-1} (ν-NO_2),[47−50] were also observed. These peaks, which did not appear for ***β*-EHS** and **R-PEP** (Figure S4A, Supporting Information), further confirm the binding of paraoxon to these monolayers. The appearance of these peaks was accompanied by the appearance of a pronounced amide I peak at 1660 cm^{-1}, suggesting assembly of the peptides into ordered and oriented parallel β-sheet structure.[51] These results indicate that paraoxon binding to ***β*-ESH** and ***β*-HES** monolayers indeed promotes peptide assembly into β-sheets, similarly to the effect observed for ***β*-ESH** in solution. The self-assembly of the β-strands in a parallel β-sheet conformation at the interface, could be expected, due to the unidirectional orientation imposed by binding the peptides on the surface through the N-terminus Cys. The appearance of small Amide II peaks at 1550 cm^{-1} further confirmed

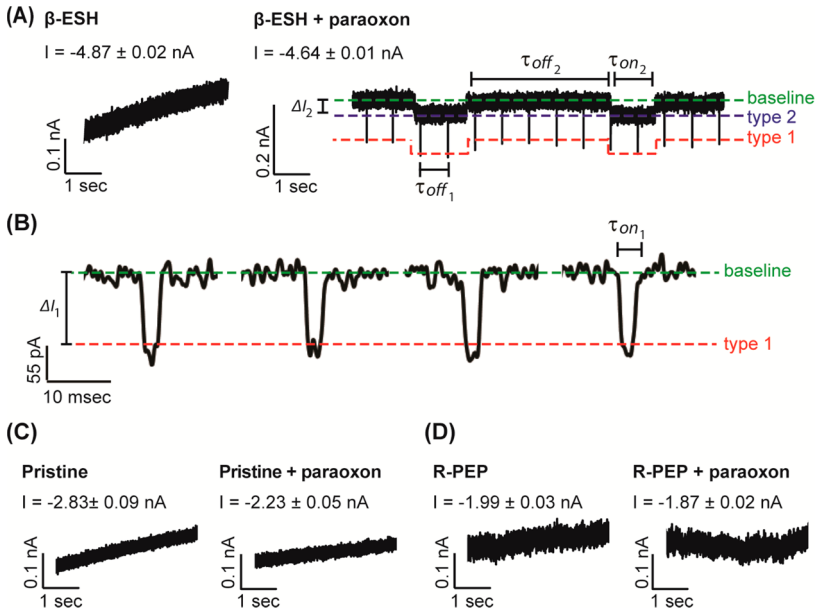

Figure 3. Current transients of peptide modified nanopores with and without paraoxon (250 μM) in the *cis*-chamber. (A) Current transient of a nanopore (average diameter ~11 nm) modified with *β*-ESH before (left) and after (right) addition of paraoxon. Type 1 and type 2 current enhancement events are marked in red and blue dashed lines, respectively. The baseline current is indicated at the top of the trace (green dashed line). (B) Zoom in on several type 1 current transient events from (A). (C,D) Control experiments showing current transients of pristine nanopore (average diameter ~9 nm) (C) and nanopore modified with R-PEP (average diameter ~16 nm) (D) before and after introduction of paraoxon to the *cis*-chamber. Ion-current traces were recorded at 500 mM KCl/55 mM TRIS·HCl buffer solution (pH = 7.4) using a voltage bias of −190 mV, low pass filter 1 kHz and data sampling rate of 12.5 kHz.

paraoxon induced ordering of the peptide monolayers. The large Amide I/Amide II peaks intensity ratio points to a large tilt angle of the peptide backbones in the β-sheet structure with respect to the surface normal. This apparent peptide tilting is in agreement with the decrease in peptide thickness, which was indicated in the ellipsometry measurements on silicon nitride (Figure 2A). Control experiments indicated that paraoxon does not adsorb directly on the gold surface (Figure S4B, Supporting Information). Additional experiments exposing substrates functionalized with L-Cys and heptanethiol further confirmed that paraoxon does not adsorb nonspecifically to charged or hydrophobic surfaces, (Figure S4B, Supporting Information). Furthermore, no significant changes in the spectra appeared for ***β*-EHS** and **R-PEP** monolayers upon exposure to paraoxon, confirming that the later did not adsorb on surfaces functionalized with these two peptides (Figure S4A, Supporting Information).

Detection of Single Paraoxon Molecule Interactions with Peptide Functionalized Nanopores. While enhancement of β-sheet formation was observed for both ***β*-ESH** and ***β*-HES** monolayers, the relative magnitude of the β-sheet related peaks in the PM-IRRAS spectra with respect to these of the paraoxon peaks were found to be larger for ***β*-ESH** monolayers (Figure 2B), indicating a more significant paraoxon induced β-sheet formation for the later. We have, therefore, decided to check whether the interactions of ***β*-ESH** with paraoxon can be detected in the context of nanopore ionic current measurements. The peptide was attached to the rims of nanopores prepared in silicon nitride membrane using the procedure described above (see also Methods section). Decrease in ionic current was manifested in the current−voltage (*I*−*V*) curves measured after each modification step (Figure S5, Supporting Information), indicating reduction in the nanopore effective diameter with each step. A general linear Ohmic behavior, especially under low biases, indicates that the tethered molecules are deposited homogeneously within the nanopore and that their conformation does not change by the electric field.[52−54]

A ***β*-ESH** modified nanopore, 11 nm average diameter, was used in order to access the ability to monitor *in situ* single paraoxon molecule binding to the monolayer by changes in the ionic current. An average current of −4.87 ± 0.02 nA was measured for the peptide functionalized nanopore using 500 mM KCl/55 mM TRIS·HCl buffer (pH = 7.4) under bias voltage of −190 mV (Figure 3A, left panel). Upon introduction of paraoxon to the *cis*-chamber at a final concentration of 250 μM, the baseline current slightly increased to a value of −4.64 ± 0.01 nA, indicating a decrease of about 5% in the total current, in similar to the 9% decrease in conductance observed in *I*−*V* measurements performed after incubating ***β*-ESH** sensitized nanopore in 250 μM paraoxon buffer solution (10 mM TRIS·HCl pH = 7.4) overnight (Figure S5C, Supporting Information). The overall reduction in the current after the addition of paraoxon to the solution was accompanied by the periodic

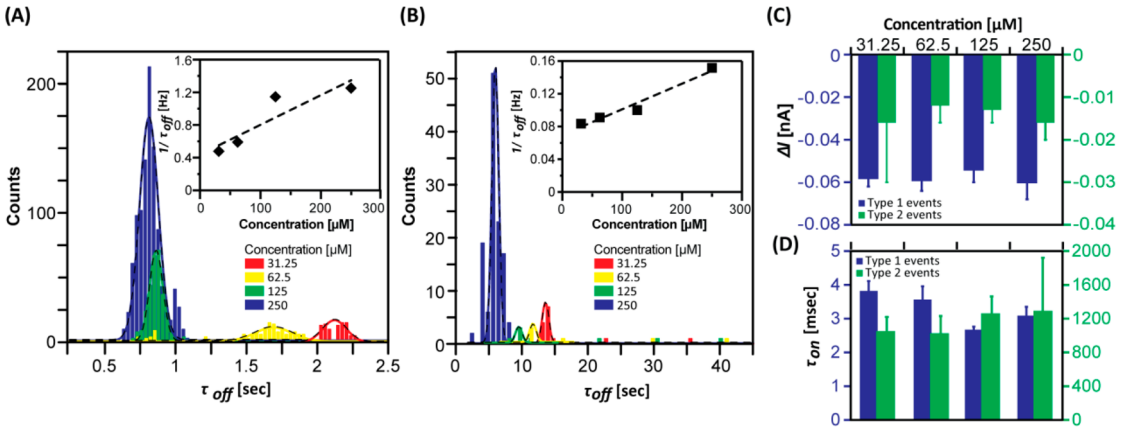

Figure 4. Influence of paraoxon concentration on events characteristics. Occurrence histograms as a function of time between events (τ_{off}) for type 1 events (A) and type 2 events (B), recorded with different paraoxon concentrations. Interevent translocation time was extracted from current time trace. Insets: dependence of event translocation rate on paraoxon concentration. A linear fit trend-line is plotted to guide the eye (dashed lines). Average values and standard deviations of pulse height, ΔI, (C) and event duration, τ_{on}, (D) for type 1 and type 2 events. Values were calculated from pulse height *versus* dwell time scatter-plots (Figure S6, Supporting Information). Transients were recorded for β-ESH modified nanopore, using paraoxon concentration ranging from 31.25 to 250 μM in 500 mM KCl/55 mM TRIS·HCl buffer (pH = 7.4), using voltage bias of −190 mV.

appearance of current enhancement events in the transient (Figure 3A, right panel). Two types of events were observed (Figure 3A,B); frequent short duration events with larger current enhancement (type 1), and less frequent longer duration events, with smaller enhancement (type 2). Occurrence frequency of both events, which will be further discussed below, was found to follow Gaussian distribution (Figure 4A,B), as expected. After thoroughly washing the fluid chamber with buffer solution, deionized water and ethanol, and refilling it with a fresh buffer solution, the current level resumed the original value measured before introduction of paraoxon, and no current enhancement events were observed. Furthermore, repeating the experiments with uncoated, pristine, nanopores (Figure 3C), and nanopores coated with **R-PEP** (Figure 3D), resulted in smooth current traces without any current enhancement or blocking events. Hence, the appearance of current enhancement events can be correlated with interactions of paraoxon with the peptide receptor layer. We note that in similar to the observed for ***β*-ESH** sensitized nanopores, the use of both pristine nanopore and a nanopore functionalize with **R-PEP** resulted in a decrease of 21 and 7% in the measured baseline current level once paraoxon was introduced to the *cis* chamber, respectively. In addition, a current drift observed for the functionalized nanopore, which was previously reported by others as well and assigned to heating,[12,55] was diminished after paraoxon addition in all cases. This behavior indicates that other interactions also occur and influence the current.

The appearance of peaks for the ***β*-ESH** sensitized nanopores cannot be explained by rapid translocation of the molecule through the nanopore and/or its loose binding to the rims since these events are not expected to induce significant changes in the current. This is supported by the fact that no peaks were observed for the pristine nanopores and for a nanopore sensitized by **R-PEP**. We, therefore, conclude that these peaks result from the extended conformational changes induced to the ***β*-ESH** monolayer by paraoxon binding that are observed in the ellipsometry and FTIR studies. These conformational changes result in a local increase in the effective size of the nanopore and thus reduce the resistance of the nanopore, leading to the observed current enhancement signal. Hence, the cooperative effect of peptide β-sheet assembly provides an effective signal amplification of paraoxon molecule binding. The appearance of two types of events with defined sizes indicates that there are two possible binding modes. The fact that type 1 event is both more frequent and is about four times larger in magnitude then type 2 event rules out the possibility that it designate simultaneous binding of several molecules, in which case the most probable event should be smaller in magnitude, and the second probable event, which should have signified the binding of two molecules should be double in size. These observations strongly indicate that each of the events is a result of two distinct interactions of a single paraoxon with the peptide monolayer. These two events do not seem to depend on each other and can occur simultaneously, as is observed in the measurements by the appearance of type 1 events with and without the background of the less frequent type 2 events.

It is important to realize that while the provided setup allows monitoring the binding of small molecules at the single molecule level, the association constant depends not only on the binding affinity of the molecule to the receptor peptide, but also on the conformational stability of the monolayer at the vicinity of the binding site. The appearance of two types of

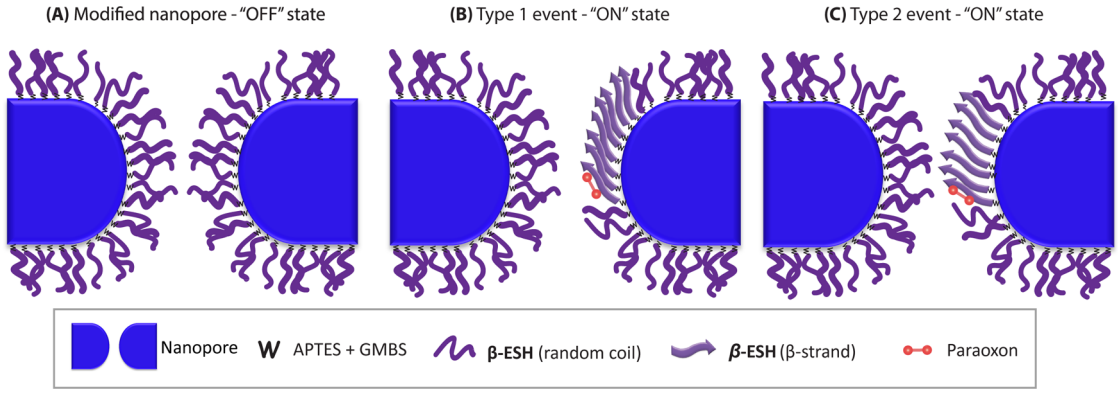

Scheme 2. Schematic representation of interactions between paraoxon and *β*-ESH sensitized nanopores. In the absence of paraoxon (OFF state) *β*-ESH adopts a random coil conformation (A). Upon introduction of paraoxon to the *cis*-side, binding to the peptide induces the formation of a β-sheet structure with large (B) or low (C) tilt angle for type 1 and type 2 events, respectively.

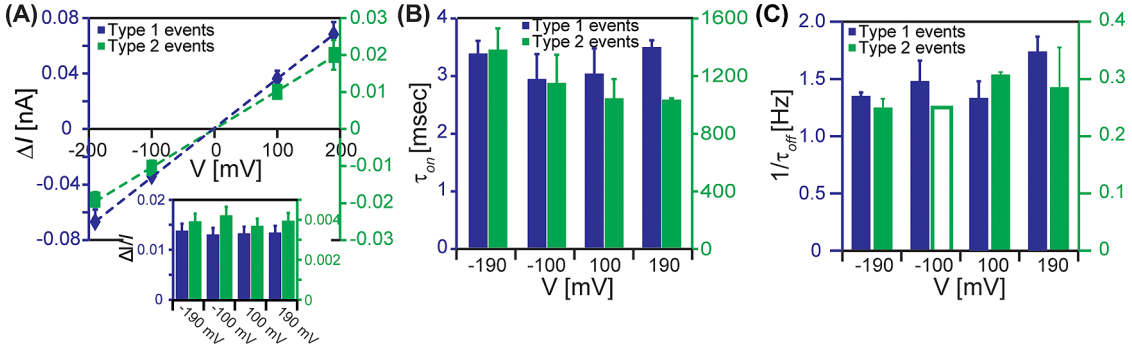

Figure 5. Influence of bias on characteristics of type 1 and type 2 current events. (A) Average values and standard deviations of the pulse height (ΔI). Inset: normalized pulse height ($\Delta I/I$, calculated as pulse height divided by the average baseline current) for each voltage. (B) Average values and standard deviations of events' duration (τ_{on}). (C) Average values and standard deviations of event rate ($1/\tau_{off}$). Data was collected for *β*-ESH modified nanopore in the presence of 250 μM paraoxon in 500 mM KCl/55 mM TRIS·HCl buffer (pH = 7.4). Values were calculated from the pulse height *versus* the dwell time (τ_{on}) scatter-plots (Figures S7 and S8, Supporting Information). Empty bar for −100 mV in (C) indicates uncertainty in the value due to the fact that only two events were recorded at this bias.

events can, accordingly, be correlated with two typical orientations of the β-sheet structure (Scheme 2). The larger enhancement of type 1 events (1.4% relative enhancement *vs* 0.004% for type 2 events) implies that in this case paraoxon binding induces a much larger tilting angle of the β-sheet structure. It is reasonable to assume that such arrangement will be much less stable due to larger spatial strain and smaller in-plane overlap between peptide molecules in the β-sheet structure. This is indeed manifested by the much shorter event duration for these events. Type 2 events, which are characterized by a β-sheet conformation with a smaller tilt angle, are indicated to be more stable. Future investigations will address this issue quantitatively.

The current enhancement events offer additional information on paraoxon interactions with the peptide monolayer. Three parameters were used to analyze events characteristics: time between adjacent events, τ_{off}; event duration, τ_{on}; and event magnitude, ΔI (these are marked in Figure 3). The effect of paraoxon concentration was investigated in the range of 31.25−250 μM. For each concentration, a time transient was recorded and both types of events were detected. For both type of events, the translocation rate, extracted as the inverse of the average value of τ_{off}, was found to be linearly dependent on the concentration (Figure 4A,B, Figure S6, Supporting Information), indicating that events rate is proportional to the concentration of paraoxon molecules in solution at this range of concentrations for both type of events. In contrary to the dependence of events rate, the magnitude of the events (Figure 4C), or their duration (Figure 4D) were found to be independent of the concentration of paraoxon. This behavior, which was previously observed for protein-receptor binding within nanopores,[14,54] is reasonable since the concentration should not affect the binding kinetics, or the resulting interactions with the peptide substrate. While the linear dependence of events frequency on the concentration could be used to quantify the concentration of paraoxon in solution in sensing applications,[1,4] the range of concentrations used in this work is far from the lower limit of detection (LLD) of 0.4 nM (10^{-7} g/L) declared by the European Union (EU) for organophosphates.[31]

Hence, further studies elucidating the detection limit, sensitivity and specificity of detection are required in order to assess the utility of these peptide functionalized nanopores as organophosphate sensors.

Further insight into event characteristics was obtained by monitoring their dependence on the bias applied between the *cis*- and *trans*-chambers (Figure 5 and Figures S7 and S8, Supporting Information). Both type of event were observed under positive as well as negative bias polarities. ΔI was found to depend linearly on the applied bias magnitude for both type of events (Figure 5A); however, the relative change of the pulse height ($\Delta I/I_0$, where I_0 is the baseline current) was found to be constant (Figure 5A, inset). This indicates that the observed change is due to changes in the rate of ion transport. Furthermore, the duration of the events was also found to be independent of the applied bias (Figure 5B). These results indicate that the interactions of paraoxon with the peptide monolayer and the peptide structure are not influenced by the bias. Finally, events' rate were also found to be independent of the bias, for both types of events (Figure 5C), indicating the lack of entropic barrier for paraoxon entering the nanopore.[11,22,56] This is probably due to the small dimensions of the paraoxon compared to the nanopore, which makes the entropic barrier presented for large DNA or polymers molecules, negligible. Hence, neither the introduction of the paraoxon into the nanopore, nor the interaction of the molecule with the receptor within the nanopore, depends on the electric field within the nanopore for both type of events.

CONCLUSIONS

We have developed a novel methodology for the detection of small molecules at the single molecule level using solid state nanopores functionalized with a monolayer of a specifically designed peptide. Our method exploits the ability to rationally design peptide receptors that undergo cooperative self-assembly and folding as a result of ligand binding. Sensitization of nanopore rims with a monolayer of such peptides induces long duration interactions of the molecules with the rims, hence matches the binding time with the temporal resolution of the measurement. Furthermore, it amplifies the signal signature by inducing a long-range conformational change in the peptide monolayer.

Specifically, we have presented here the design of a peptide with a receptor unit for paraoxon, inspired by the catalytic triad of AChE. The amino acid triad is embedded within the hydrophilic plane of a β-sheet forming peptide. The self-assembly of the peptide into a β-sheet structure was shown to be promoted by paraoxon binding both in solution and for peptide monolayers, depending on the order of the amino acids triad in the sequence. Single molecule interactions of paraoxon with a monolayer of the peptide attached to the rims of nanopores could be detected as peaks in ionic current passing through the nanopore, due to an increase in the effective diameter of the nanopore as a result of the formation of a β-sheet structure tilted with respect to the nanopore surface. The sensitivity of the method has been demonstrated by the ability to detect two types of interactions, differing in the tilt angle and the binding constant. The ability to detect organophosphate molecules makes this method very important for environmental and warfare applications. Furthermore, this method is very versatile and can be used for the detection of any molecule, provided that a proper peptide receptor is designed. Hence, the suggested concept can be used for the development of highly sensitive small molecule sensors. Moreover, the system can be used to study receptor−small molecule interactions with high sensitivity at the single molecule level.

METHODS

Peptides and Reagents. Peptides (1201.37 g/mol) with purity above 95% were purchased from GenScript (Piscataway, NJ). HPLC grade acetonitrile and ethanol were purchased from J.T. Baker (Beit-Dekel, Israel). Sulfo-GMBS was supplied by Pierce (Rockford, IL). For silanization, ethanol was dried over magnesium sulfate and kept dried using 3 Å molecular sieves until use. Paraoxon, dimethyl sulfoxide (DMSO), (3-aminopropyl)-triethoxysilane (APTES) and Tris(2-carboxyethyl)phosphine hydrochloride (TCEP) were purchased from Sigma-Aldrich (Rehovot, Israel) and used as received. Phosphate buffer (PB) (100 mM; 12 g/L NaH_2PO_4, 14.2 g/L Na_2HPO_4) and 10 mM TRIS·HCl buffer (1.2 g/L TRIS·HCl) were prepared and adjusted to pH 7.4 with NaOH/HCl.

Circular Dichroism (CD). CD measurements were performed on a Jasco J-715 spectropolarimeter (Jasco, Inc., Easton, MD) using Quartz cuvettes with 1.0 mm path length. Data was collected in 180−250 nm wavelength range at 20 °C, with bandwidth of 1 nm, in continuous mode with 0.5 nm steps, 4 s response time, and scan speed of 50 nm/min. Spectra are reported as mean molar ellipticity [θ_{mr}, deg·cm^2·dmol^{-1}·res^{-1}] *versus* wavelength. CD spectra were recorded for peptides concentration of 0.12 mg/mL (100 μM). Each peptide was first dissolved in acetonitrile and sonicated for 10 min, followed by addition of an equal volume of deionized water or the paraoxon solution diluted in deionized water. The final concentration of paraoxon was 2.5−250 μM. Solutions with same concentration of paraoxon were used as references, eliminating possible effect of the paraoxon on the spectrum.

Silicon Nitride Surface Functionalization. Surface functionalization of silicon nitride samples is shown in Figure 2 and Scheme S1 (Supporting Information). Phosphorus doped *n*-Type Si wafers ((100), 1−10 Ω·cm resistivity) with a top 30 nm thick silicon nitride layer prepared by low pressure chemical vapor deposition (LPCVD) were purchased from Virginia Semiconductor, Inc. (Fredericksburg, VA). Silicon nitride surfaces were cleaned in piranha solution (7:3 (v/v) concentrated sulfuric acid:30% hydrogen peroxide) for 30 min at 90 °C, followed by triple washing (10 min each) in deionized water. (*Caution! Piranha solution is highly corrosive and very dangerous*

and should be handled with care.) Samples were dried under nitrogen flow. Immediately after, samples were immersed in freshly prepared solution of 5% (v/v) APTES in dried ethanol under nitrogen atmosphere for 10 min, followed by triple wash in ethanol (10 min each), drying under N_2 stream and baking at 110 °C for 30 min.[45] Samples were immersed in 3 mM sulfo-GMBS/100 mM PB. After 1 h. the solution was removed and samples were soaked three times for 10 min each in PB and dried under N_2 stream.[30] The maleimide modified samples were immersed in freshly prepared 0.5 mM peptide solution (peptides were dissolved in DMSO to a concentration of 2.5 mM, and were further diluted to 0.5 mM solution in 4 mM TCEP/100 mM PB) for 3 h, washed three times in PB and deionized water (10 min each) and dried under N_2 stream.

Gold Samples Surface Functionalization. Gold samples were prepared by sputtering 200 nm thick Gold films on Si (100) wafers (Virginia Semiconductor, Inc., Fredericksburg, VA), using Cr (8 nm) adhesion layer (ODEM sputter system, 4×10^{-9} mbar base pressure). Prior to peptide assembly samples were cleaned by sonication in ethanol bath for 15 min, hydrogen flame annealed, and were treated by ozone/UV for 20 min at 40 °C (PCD-UVT, Novascan, AMES, IA). Samples were then sonicated in ethanol bath for 15 min, and dried under N_2 flow.[57] Immediately after, samples were immersed in fresh 0.5 mM peptide solution in 100 mM PB for 3 h. Thereafter, samples were incubated in 500 μM paraoxon solution in TRIS·HCl buffer (pH = 7.4) for 8 h. After each step, excess of material was removed by gently shaking for 10 min in PB and deionized water three times, and drying under N_2 stream. Layer thickness was calculated from ellipsometry measurements performed using PHE101 Ellipsometer (Angstrom Advanced, Inc., Braintree, MA) at a wavelength of 632.8 nm and angle of 70°. Refractive index of 1.5 was used for all organic substances.

Polarization Modulation Infrared Reflection/Adsorption Spectroscopy (PM-IRRAS). PM-IRRAS characterizations were obtained on peptide modified gold samples using Nicolet 6700 spectrophotometer equipped with a liquid nitrogen-cooled MCT detector (Thermo, Madison, WI). The detector angle was set to 85° (initial experiments have shown maximal signal-to-noise ratio at this angle), the modulation frequency was set at 1600 cm^{-1} and 400 scans at a resolution of 8 cm^{-1} were collected for each spectrum. The incident IR beam was polarized by ZnSe polarizer between parallel (*p*) and perpendicular (*s*) polarization to the plane of incident. The signal was processed and reported as the differential reflectivity spectrum $\Delta R/R = (R_p - R_s)/(R_p + R_s)$, where R_p and R_s are the polarized reflectivities for *p* and *s* polarizations, respectively. Background subtraction was obtained by removing the spectra of a clean gold surface. Spectra were normalized and smoothed using the Omnic software (Thermo, Madison, WI).

Nanopore Fabrication. Nanopores were fabricated in plasma cleaned (Ar gas) 30 nm thick silicon nitride membranes (window size 50·50 μm^2) supported by a 300 μm thick Si frame (Protochips, Inc., Raleigh, NC). The nanopores were drilled using a high intensity focused electron beam based on previously reported procedures.[58,59] In brief, a single nanopore was drilled in each membrane using a converged beam of a high resolution transmission electron microscopy (HR-TEM) with an incident accelerating voltage of 200 kV from FEG source (JEOL, 2100F). The microscope was operated in converged beam diffraction mode (CBD, 2.4 nm beam diameter) and at 400 K magnification. Plan-view TEM imaging was used to monitor the size of the nanopores. An average diameter was extracted from the area of the nanopore, which was evaluated by pixel counting using ImageJ software. The drilling process has begun with a nanopore opening, typically 8 nm in diameter, by a direct illumination of the sample for 1 min. Thereafter, the beam was gently moved on the pore−vacuum interface to enlarge the pore up to the desired size, between 10 to 30 nm diameter in average.

Nanopore Modification. Chips containing the nanopores were cleaned by ozone treatment (PCD-UVT, Novascan, AMES, IA) for 1 min from each side and immediately soaked in 1:1 ethanol: triple deionized water solution for a day. This allowed proper wetting of the pore region and therefore improved ions and analyte translocations. Surface modifications were obtained using the procedure used for silicon nitride surface modifications.[54] N_2 dried chips were suspended in freshly prepared 5% (v/v) APTES/ethanol solution for 10 min under nitrogen atmosphere, followed by washing in ethanol, and drying under N_2 stream. Samples where then baked at 110 °C for 30 min and after cooling to room temperature immersed for 1 h. in 3 mM sulfo-GMBS linker in 100 mM PB. For creating the thioether bond with the peptide, samples were immersed for 3 h. in 0.5 mM ***β*-ESH**/4 mM TCEP/100 mM PB containing 20% (v/v) DMSO. Paraoxon was introduced to the nanopore by incubating the chip in solution of 250 μM paraoxon in 10 mM TRIS·HCl buffer (pH = 7.4) overnight. This pH was used to match the binding conditions as much as possible to the physiological conditions, at which AchE is active. After each modification step, the chip was gently agitated five times (10 min each) with the pure solvent that was used during the modification step. Modifications were validated by a decrease in the ionic conductance. Prior to electrical characterizations samples were kept for few hours in 1:1 ethanol:triple deionized water solution.

Electrical Measurements. Clean or modified chips were mounted between two Teflon gaskets separating two Teflon reservoirs, filled with KCl solution (250−1000 mM in 10 mM Tris·HCl buffer (pH = 7.4)) and equipped with Ag/AgCl electrodes connected to an Axopatch 200B amplifier that was controlled by the pClamp software (Axon Instruments, Sunnyvale, CA). The measurements were recorded using a low pass Bessel filter of 5 kHz and data sampling rate of 12.5 kHz. For *I*−*V* measurements the DC current was measured as a function of the applied voltage, which was stepped between −190 and 190 mV with 10 mV intervals every 0.25 s. The conductance of the nanopore was calculated from the slope of the curve. For statistical analysis, different nanopores were measured for each step ($n = 3-6$). For paraoxon translocation experiments, each of the reservoirs was filled with 500 mM KCl/55 mM TRIS·HCl buffer pH = 7.4, and the paraoxon was added to the *cis*-side of the cell to a final concentration of 250 μM. Serial dilutions were done in the cell to dilute the paraoxon down to 31.25 μM by adding a corresponding volume of 55 mM TRIS·HCl buffer (pH 7.4). The measurements were recorded using a low pass Bessel filter (1 kHz) and data sampling rate of 12.5 kHz at an applied voltage of −190 mV, unless otherwise noted. All data were analyzed using Clampfit software (Axon Instruments, Sunnyvale, CA). Translocation events were detected by threshold search procedure, and only events exceeding three times the standard deviation of the noise were accepted. Each experiment was repeated successfully at least three times, and representative results are shown.

Conflict of Interest: The authors declare no competing financial interest.

Acknowledgment. We thank Prof. A. Kushmaro for providing the paraoxon solutions, and Drs. V. Ezersky, S. Kolusheva, and N. Frumin from the Ilse Katz Institute for Nanoscale Science and Technology (IKI, Ben Gurion University) for their assistance in TEM, PM-IRRAS and XPS operation. Y.L.P. is a recipient of a Negev doctoral scholarship and the Shimona Geresh prize. Part of this work was financially supported by a DIP Grant (AS 424/1-1).

Supporting Information Available: Additional CD spectra; characterizations of peptide monolayers on gold and silicon nitride, including contact angle and XPS data, and additional ellipsometry and PM-IRRAS characterizations; nanopores' *I*−*V* curves and voltage-dependent ion current transient analysis histograms. This material is available free of charge *via* the Internet at http://pubs.acs.org.

REFERENCES AND NOTES

1. Kasianowicz, J. J.; Robertson, J. W. F.; Chan, E. R.; Reiner, J. E.; Stanford, V. M. Nanoscopic Porous Sensors. *Annu. Rev. Anal. Chem.* **2008**, *1*, 737–766.
2. Henriquez, R. R.; Ito, T.; Sun, L.; Crooks, R. M. The Resurgence of Coulter Counting for Analyzing Nanoscale Objects. *Analyst* **2004**, *129*, 478–482.
3. Schmidt, J. Stochastic Sensors. *J. Mater. Chem.* **2005**, *15*, 831–840.

4. Howorka, S.; Siwy, Z. Nanopore Analytics: Sensing of Single Molecules. *Chem. Soc. Rev.* **2009**, *38*, 2360–2384.
5. Martin, C. R.; Siwy, Z. S. Learning Nature's Way: Biosensing with Synthetic Nanopores. *Science* **2007**, *317*, 331–332.
6. Majd, S.; Yusko, E. C.; Billeh, Y. N.; Macrae, M. X.; Yang, J.; Mayer, M. Applications of Biological Pores in Nanomedicine, Sensing, and Nanoelectronics. *Curr. Opin. Biotechnol.* **2010**, *21*, 439–476.
7. Bayley, H.; Cremer, P. S. Stochastic Sensors Inspired by Biology. *Nature* **2001**, *413*, 226–230.
8. Rhee, M.; Burns, M. A. Nanopore Sequencing Technology: Nanopore Preparations. *Trends Biotechnol.* **2007**, *25*, 174–181.
9. Dekker, C. Solid-State Nanopores. *Nat. Nanotechnol.* **2007**, *2*, 209–215.
10. Branton, D.; Deamer, D. W.; Marziali, A.; Bayley, H.; Benner, S. A.; Butler, T.; Di Ventra, M.; Garaj, S.; Hibbs, A.; Huang, X. H.; *et al.* The Potential and Challenges of Nanopore Sequencing. *Nat. Biotechnol.* **2008**, *26*, 1146–1153.
11. Wanunu, M. Nanopores: A Journey Towards DNA Sequencing. *Phys. Life Rev.* **2012**, *9*, 125–158.
12. Han, A.; Creus, M.; Schurmann, G.; Linder, V.; Ward, T. R.; de Rooij, N. F.; Staufer, U. Label-Free Detection of Single Protein Molecules and Protein-Protein Interactions Using Synthetic Nanopores. *Anal. Chem.* **2008**, *80*, 4651–4658.
13. Talaga, D. S.; Li, J. L. Single-Molecule Protein Unfolding in Solid State Nanopores. *J. Am. Chem. Soc.* **2009**, *131*, 9287–9297.
14. Sexton, L. T.; Horne, L. P.; Sherrill, S. A.; Bishop, G. W.; Baker, L. A.; Martin, C. R. Resistive-Pulse Studies of Proteins and Protein/Antibody Complexes Using a Conical Nanotube Sensor. *J. Am. Chem. Soc.* **2007**, *129*, 13144–13152.
15. Wei, R.; Gatterdam, V.; Wieneke, R.; Tampe, R.; Rant, U. Stochastic Sensing of Proteins with Receptor-Modified Solid-State Nanopores. *Nat. Nanotechnol.* **2012**, *7*, 257–263.
16. Venkatesan, B. M.; Bashir, R. Nanopore Sensors for Nucleic Acid Analysis. *Nat. Nanotechnol.* **2011**, *6*, 615–624.
17. Boersma, A. J.; Brain, K. L.; Bayley, H. Real-Time Stochastic Detection of Multiple Neurotransmitters with a Protein Nanopore. *ACS Nano* **2012**, *6*, 5304–5308.
18. Clamer, M.; Höfler, L.; Mikhailova, E.; Viero, G.; Bayley, H. Detection of 3′-End Rna Uridylation with a Protein Nanopore. *ACS Nano* **2013**, *8*, 1364–1374.
19. Jayawardhana, D. A.; Crank, J. A.; Zhao, Q.; Armstrong, D. W.; Guan, X. Y. Nanopore Stochastic Detection of a Liquid Explosive Component and Sensitizers Using Boromycin and an Ionic Liquid Supporting Electrolyte. *Anal. Chem.* **2009**, *81*, 460–464.
20. Wang, H.-Y.; Ying, Y.-L.; Li, Y.; Kraatz, H.-B.; Long, Y.-T. Nanopore Analysis of B-Amyloid Peptide Aggregation Transition Induced by Small Molecules. *Anal. Chem.* **2011**, *83*, 1746–1752.
21. Wang, Y.; Zheng, D.; Tan, Q.; Wang, M. X.; Gu, L. Q. Nanopore-Based Detection of Circulating Micrornas in Lung Cancer Patients. *Nat. Nanotechnol.* **2011**, *6*, 668–674.
22. Anderson, B. N.; Muthukumar, M.; Meller, A. Ph Tuning of DNA Translocation Time through Organically Functionalized Nanopores. *ACS Nano* **2013**, *7*, 1408–14.
23. Tian, Y.; Hou, X.; Wen, L.; Guo, W.; Song, Y.; Sun, H.; Wang, Y.; Jiang, L.; Zhu, D. A Biomimetic Zinc Activated Ion Channel. *Chem. Commun.* **2010**, *46*, 1682–1684.
24. Boersma, A. J.; Bayley, H. Continuous Stochastic Detection of Amino Acid Enantiomers with a Protein Nanopore. *Angew. Chem.* **2012**, *124*, 9744–9747.
25. Kawano, R.; Osaki, T.; Sasaki, H.; Takinoue, M.; Yoshizawa, S.; Takeuchi, S. Rapid Detection of a Cocaine-Binding Aptamer Using Biological Nanopores on a Chip. *J. Am. Chem. Soc.* **2011**, *133*, 8474–8477.
26. Ying, Y. L.; Zhang, J.; Meng, F. N.; Cao, C.; Yao, X.; Willner, I.; Tian, H.; Long, Y. T. A Stimuli-Responsive Nanopore Based on a Photoresponsive Host-Guest System. *Sci. Rep.* **2013**, *3*, 1662.
27. Millard, C. B.; Kryger, G.; Ordentlich, A.; Greenblatt, H.; Harel, M.; Raves, M. L.; Segall, Y.; Barak, D.; Shafferman, A.; Silman, A.; *et al.* Crystal Structures of Aged Phosphorylated Acetylcholinesterase Nerve Agent Reaction Products at Atomic Level. *Biochemistry* **1999**, *38*, 7032–7039.
28. Sussman, J. L.; Harel, M.; Silman, I. Three Dimensional Structure of Acetylcholinesterase and of Its Complexes with Anticholine Drugs. *Chem. Biol. Interact.* **1993**, *87*, 187–197.
29. Schulze, H.; Vorlová, S.; Villatte, F.; Bachmann, T. T.; Schmid, R. D. Design of Acetylcholinesterases for Biosensor Applications. *Biosens. Bioelectron.* **2003**, *18*, 201–209.
30. Singh, A. K.; Flounders, A. W.; Volponi, J. V.; Ashley, C. S.; Wally, K.; Schoeniger, J. S. Development of Sensors for Direct Detection of Organophosphates. Part I: Immobilization, Characterization and Stabilization of Acetylcholinesterase and Organophosphate Hydrolase on Silica Supports. *Biosens. Bioelectron.* **1999**, *14*, 703–13.
31. Van Dyk, J. S.; Pletschke, B. Review on the Use of Enzymes for the Detection of Organochlorine, Organophosphate and Carbamate Pesticides in the Environment. *Chemosphere* **2011**, *62*, 291–307.
32. Martinez, R. C.; Gonzalo, E. R.; Moran, M. J. A.; Mendez, J. H. Sensitive Method for the Determination of Organophosphorus Pesticides in Fruits and Surface Waters by High-Performance Liquid Chromatography with Ultraviolet Detection. *J. Chromatogr. A* **1992**, *607*, 37–45.
33. Pylypiw, H. M. Rapid Gas Chromatographic Method for the Multiresidue Screening of Fruits and Vegetables for Organochlorine and Organophosphate Pesticides. *J. AOAC Int.* **1993**, *76*, 1369–1373.
34. Elhanany, E.; Ordentlich, A.; Dgany, O.; Kaplan, D.; Segall, Y.; Barak, R.; Velan, B.; Shafferman, A. Resolving Pathways of Interaction of Covalent Inhibitors with the Active Site of Acetylcholinesterases: Maldi-Tof/Ms Analysis of Various Nerve Agent Phosphyl Adducts. *Chem. Res. Toxicol.* **2001**, *14*, 912–918.
35. Andreescu, D.; Marty, J. L. Twenty Years Research in Cholinesterase Biosensors: From Basic Research to Practical Applications. *Biomol. Eng.* **2006**, *23*, 1–15.
36. Arduini, F.; Amine, A.; Moscone, D.; Palleschi, G. Biosensors Based on Cholinesterase Inhibition for Insecticides, Nerve Agents and Aflatoxin B1 Detection (Review). *Microchim. Acta* **2010**, *170*, 193–214.
37. Liu, S.; Yuan, L.; Yue, X.; Zheng, Z.; Tang, Z. Recent Advances in Nanosensors for Organophosphate Pesticide Detection. *Adv. Powder Technol.* **2008**, *19*, 419–441.
38. Skladal, P. Biosensors Based on Cholinesterase for Detection of Pesticides. *Food Technol. Biotechnol.* **1996**, *34*, 43–49.
39. Yaakobi, K.; Liebes-Peer, Y.; Kushmaro, A.; Rapaport, H. Designed Amphiphilic B-Sheet Peptides Monolayers for Sensing the Organophosphate Paraoxon. *Langmuir* **2013**, *29*, 6840–6848.
40. Rapaport, H. Ordered Peptide Assemblies at Interfaces. *Supramol. Chem.* **2006**, *18*, 445–454.
41. Rapaport, H.; Kjaer, K.; Jensen, T. R.; Leiserowitz, L.; Tirrell, D. A. Two-Dimensional Order in β-Sheet Peptide Monolayers. *J. Am. Chem. Soc.* **2000**, *122*, 12523–12529.
42. Adler-Abramovich, L.; Reches, M.; Sedman, V. L.; Allen, S.; Tendler, S. J. B.; Gazit, E. Thermal and Chemical Stability of Diphenylalanine Peptide Nanotubes: Implications for Nanotechnological Applications. *Langmuir* **2006**, *22*, 1313–1320.
43. Roy, R. S.; Gopi, H. N.; Raghothama, S.; Gilardi, R. D.; Karle, I. L.; Balaram, P. Peptide Hairpins with Strand Segments Containing α- and β-Amino Acid Residues: Cross-Strand Aromatic Interactions of Facing Phe Residues. *Biopolymers* **2005**, *80*, 787–99.
44. Castelletto, V.; Hamley, I. W. Self Assembly of a Model Amphiphilic Phenylalanine Peptide/Polyethylene Glycol Block Copolymer in Aqueous Solution. *Biophys. Chem.* **2009**, *141*, 169–74.
45. Aswal, D. K.; Lenfant, S.; Guerin, D.; Yakhmi, J. V.; Vuillaume, D. Self Assembled Monolayers on Silicon for Molecular Electronics. *Anal. Chem. Acta* **2006**, *568*, 84–108.
46. Segman-Magidovich, S.; Grisaru, H.; Gitli, T.; Levi-Kalisman, Y.; Rapaport, H. Matrices of Acidic β-Sheet Peptides as Templates for Calcium Phosphate Mineralization. *Adv. Mater.* **2008**, *20*, 2156–2161.

47. Wang, C.; Zheng, J.; Oliveira, O. N.; Leblanc, R. M. Nature of the Interaction between a Peptidolipid Langmuir Monolayer and Paraoxon in the Subphase. *J. Phys. Chem. C* **2007**, *111*, 7826–7833.
48. Zheng, J.; Desbat, B.; Rastogi, V. K.; Shah, S. S.; DeFrank, J. J.; Leblanc, R. M. Organophosphorus Hydrolase at the Air–Water Interface: Secondary Structure and Interaction with Paraoxon. *Biomacromolecules* **2006**, *7*, 2806–2810.
49. Dziri, L.; Desbat, B.; Leblanc, R. M. Polarization-Modulated Ft-Ir Spectroscopy Studies of Acetylcholinesterase Secondary Structure at the Air–Water Interface. *J. Am. Chem. Soc.* **1999**, *121*, 9618–9625.
50. Kim, S. H.; Kim, J. H.; Kang, B.-K. Decomposition Reaction of Organophosphorus Nerve Agents on Solid Surfaces with Atmospheric Radio Frequency Plasma Generated Gaseous Species. *Langmuir* **2007**, *23*, 8074–8078.
51. Sneer, R.; Weygand, M. J.; Kjaer, K.; Tirrell, D. A.; Rapaport, H. Parallel B-Sheet Assemblies at Interfaces. *ChemPhysChem* **2004**, *5*, 747–750.
52. Siwy, Z. S. Ion-Current Rectification in Nanopores and Nanotubes with Broken Symmetry. *Adv. Funct. Mater.* **2006**, *16*, 735–746.
53. Mussi, V.; Fanzio, P.; Repetto, L.; Firpo, G.; Scaruffi, P.; Stigliani, S.; Tonini, G. P.; Valbusa, U. DNA-Functionalized Solid State Nanopore for Biosensing. *Nanotechnology* **2010**, *21*, 145102.
54. Kowalczyk, S. W.; Kapinos, L.; Blosser, T. R.; Magalhaes, T.; van Nies, P.; LimRoderick, Y. H.; Dekker, C. Single-Molecule Transport across an Individual Biomimetic Nuclear Pore Complex. *Nat. Nanotechnol.* **2011**, *6*, 433–438.
55. Ding, S.; Gao, C.; Gu, L. Q. Capturing Single Molecules of Immunoglobulin and Ricin with an Aptamer-Encoded Glass Nanopore. *Anal. Chem.* **2009**, *81*, 6649–6655.
56. Muthukumar, M. Mechanism of DNA Transport through Pores. *Annu. Rev. Biophys. Biomol. Struct.* **2007**, *36*, 435–450.
57. Nogues, C.; Wanunu, M. A Rapid Approach to Reproducible, Atomically Flat Gold Films on Mica. *Surf. Sci.* **2004**, *573*, L383–L389.
58. Kim, M. J.; Wanunu, M.; Bell, D. C.; Meller, A. Rapid Fabrication of Uniformly Sized Nanopores and Nanopore Arrays for Parallel DNA Analysis. *Adv. Mater.* **2006**, *18*, 3149–3153.
59. Ho, C.; Qiao, R.; Heng, J. B.; Chatterjee, A.; Timp, R. J.; Aluru, N. R.; Timp, G. Electrolytic Transport through a Synthetic Nanometer-Diameter Pore. *Proc. Natl. Acad. Sci. U. S. A.* **2005**, *102*, 10445–10450.